



# UWB-enabled Sensing for Fast and Effortless Blood Pressure Monitoring

ZHI WANG, Institute of Software, Chinese Academy of Sciences and University of Chinese Academy of Sciences, China

BEIHONG JIN, Institute of Software, Chinese Academy of Sciences and University of Chinese Academy of Sciences, China

FUSANG ZHANG, Institute of Software, Chinese Academy of Sciences and University of Chinese Academy of Sciences, China

SIHENG LI, Institute of Software, Chinese Academy of Sciences and University of Chinese Academy of Sciences, China

JUNQI MA, Institute of Software, Chinese Academy of Sciences and University of Chinese Academy of Sciences, China

Blood Pressure (BP) is a critical vital sign to assess cardiovascular health. However, existing cuff-based and wearable-based BP measurement methods require direct contact between the user's skin and the device, resulting in poor user experience and limited engagement for regular daily monitoring of BP. In this paper, we propose a contactless approach using Ultra-WideBand (UWB) signals for regular daily BP monitoring. To remove components of the received signals that are not related to the pulse waves, we propose two methods that utilize peak detection and principal component analysis to identify aliased and deformed parts. Furthermore, to extract BP-related features and improve the accuracy of BP prediction, particularly for hypertensive users, we construct a deep learning model that extracts features of pulse waves at different scales and identifies the different effects of features on BP. We build the corresponding BP monitoring system named RF-BP and conduct extensive experiments on both a public dataset and a self-built dataset. The experimental results show that RF-BP can accurately predict the BP of users and provide alerts for users with hypertension. Over the self-built dataset, the mean absolute error (MAE) and standard deviation (SD) for SBP are 6.5 mmHg and 6.1 mmHg, and the MAE and SD for DBP are 4.7 mmHg and 4.9 mmHg.

CCS Concepts: • Human-centered computing → Ubiquitous and mobile computing systems and tools.

Additional Key Words and Phrases: Contactless sensing; UWB signals; Blood pressure; Hypertension

## ACM Reference Format:

Zhi Wang, Beihong Jin, Fusang Zhang, Siheng Li, and Junqi Ma. 2024. UWB-enabled Sensing for Fast and Effortless Blood Pressure Monitoring. *Proc. ACM Interact. Mob. Wearable Ubiquitous Technol.* 8, 2, Article 65 (June 2024), 26 pages.

<https://doi.org/10.1145/3659617>

## 1 INTRODUCTION

Blood pressure (BP) generally refers to arterial blood pressure, which is the force of the blood that pushes against the walls of the arteries as blood flows. As one of the fundamental vital signs, BP plays a crucial role in

---

Authors' addresses: **Zhi Wang**, Key Laboratory of System Software (Chinese Academy of Sciences) and State Key Laboratory of Computer Science, Institute of Software, Chinese Academy of Sciences; E-mail: wangzhi20@otcaix.icas.ac.cn. **Beihong Jin**, Key Laboratory of System Software (Chinese Academy of Sciences) and State Key Laboratory of Computer Science, Institute of Software, Chinese Academy of Sciences; E-mail: beihong@iscas.ac.cn. **Fusang Zhang**, Key Laboratory of System Software (Chinese Academy of Sciences) and State Key Laboratory of Computer Science, Institute of Software, Chinese Academy of Sciences; E-mail: zhangfusang@otcaix.icas.ac.cn. **Siheng Li**, Key Laboratory of System Software (Chinese Academy of Sciences) and State Key Laboratory of Computer Science, Institute of Software, Chinese Academy of Sciences; E-mail: lisiheng19@otcaix.icas.ac.cn. **Junqi Ma**, Key Laboratory of System Software (Chinese Academy of Sciences) and State Key Laboratory of Computer Science, Institute of Software, Chinese Academy of Sciences; E-mail: majunqi22@otcaix.icas.ac.cn. Corresponding author: Beihong Jin.

---

Permission to make digital or hard copies of all or part of this work for personal or classroom use is granted without fee provided that copies are not made or distributed for profit or commercial advantage and that copies bear this notice and the full citation on the first page. Copyrights for components of this work owned by others than the author(s) must be honored. Abstracting with credit is permitted. To copy otherwise, or republish, to post on servers or to redistribute to lists, requires prior specific permission and/or a fee. Request permissions from permissions@acm.org.

© 2024 Copyright held by the owner/author(s). Publication rights licensed to ACM.

ACM 2474-9567/2024/5-ART65

<https://doi.org/10.1145/3659617>



Fig. 1. Blood pressure monitoring.

assessing the normal functioning of the heart, blood flow, blood volume, and vascular diastolic function in humans. Deviations from the normal BP range can indicate underlying health problems. High BP might be associated with coronary heart disease, cerebrovascular disease, and other diseases, while low BP can lead to symptoms such as palpitations, fatigue, dizziness, and cardiovascular disorders. Notably, hypertension is a significant cause of premature death worldwide. According to the global trends in hypertension prevalence and progress, the number of people aged 30-79 years with hypertension doubled between 1990 and 2019, with nearly half of them remaining unaware of their condition [65]. Additionally, raised BP is estimated to cause 7.5 million deaths worldwide, about 12.8% of the total of all deaths [11]. Facing this alarming situation, regular daily monitoring of BP is of critical importance, which can not only indicate hypertensive users to take the medication but also deliver timely alerts for cases of malignant hypertension [30].

Conventional BP measurement methods primarily rely on cuff-based techniques. As shown in Figure 1a, auscultation is the standard BP measurement method. When measuring BP, a balloon is inflated and pressurized into a cuff wrapped around the upper arm, and the applied pressure is transmitted to the brachial artery through the surrounding soft tissues. Then, the balloon is slowly deflated, during which the pulse sounds are detected with a stethoscope to obtain the systolic blood pressure (SBP) and diastolic blood pressure (DBP). Oscillometry, an automatic measurement method, is currently the most widely used in clinical practice, as shown in Figure 1b. While cuff-based BP measurement methods can accurately measure a user's BP, the pressure on the upper arm from the cuff can induce discomfort for the individual and the process needs assistance from others. As a result, numerous people do not check their BP as required, and therefore are not aware of their hypertensive condition or are not motivated enough to take their antihypertensive medications.

In order to enhance the convenience of BP monitoring, existing work focuses on extracting BP-related features from radio or optical signals using various sensing devices, resulting in two categories of BP measurement methods: wearable and contactless methods.

Currently, some smart watches [3, 5] provide the BP measurement. The BP can be estimated by receiving the signals obtained by the built-in optical heart rate sensor or ECG sensor and extracting features related to pulse waves such as pulse transit time (PTT), pulse wave velocity (PWV) and pulse arrival time (PAT) [16, 19, 26, 41]. However, the accuracy is compromised when the watch is not in good contact with the skin. Furthermore, all of smart watches are required to directly contact with the user's skin, which is not suitable for users with skin allergies, skin trauma, or skin burns. In terms of user experience, the smart watches are not suitable for regular daily monitoring of BP.

In recent years, wireless sensing has made significant advancements in vital sign monitoring, including contactless respiration rate monitoring [56, 66], heart rate monitoring [32, 47], apnea recognition [34, 35], heartbeat waveform extraction [22, 63], and electrocardiogram generation [59]. Wireless signals such as Wi-Fi,

RFID, and radar have demonstrated effectiveness in monitoring vital signs. However, Wi-Fi is unable to achieve high distance resolution due to its limited bandwidth, which makes it difficult to get heartbeat information and further infer blood pressure. The low frequency of RFID signals results in small phase changes during pulse wave measurements, rendering them susceptible to noise interference. Also, RFID typically requires the attachment of a tag to the user's clothing to measure vital sign, which brings noise to the received signals and makes it difficult to extract features related to pulse waves. Radar signals have good performance in terms of resolution, stability, and interference resistance, so they are favored by researchers in industry and academia. To measure BP in a contactless manner, researchers have tried different wireless signals such as continuous wave (CW) signals, frequency modulation continuous wave (FMCW) signals, and ultra-wideband (UWB) signals. By analyzing the signals reflected off the human body, researchers can extract features of pulse waves for blood pressure estimation. However, despite the significant progress in contactless vital sign monitoring, research efforts to measure BP in a contactless manner are relatively limited.

Among all the radar based signals, we choose UWB signals to monitor BP. One reason for choosing UWB signals is that they exhibit fewer harmonics and a higher signal-to-noise ratio (SNR) compared to FMCW signals. CW signals do not have the ability to measure the distance between the user and the device, leading to CW signals not being able to eliminate interferences caused by reflection from other objects and multi-path reflection. Another reason is the increasing integration of UWB chips in smart devices. Many smart phones such as Apple iPhone, Samsung Galaxy, Google Pixel, and Xiaomi MIX4 have integrated UWB chips [2, 4, 10, 12]. Furthermore, the latest smart watches and smart speakers also have integrated UWB chips [8]. The availability of a large number of commercial UWB chips has made it possible to commercialize UWB signal-based BP monitoring in real-world applications.

A typical scenario for BP monitoring is that a user sits at a desk and the UWB device is placed in front of the user, as shown in Figure 1c. The UWB device sends pulse signals to the human body. During this period, the user can read a book, write by hand, use a computer, move the mouse or hit the keyboard, etc. By analyzing and mining the reflected signals, the user's BP is expected to be obtained. This process does not require a deep involvement of the user.

However, for accurately predicting BP from received UWB signals, two challenges need to be addressed. Firstly, the received signals are widely perceived as containing human movements, respiration, pulse waves, etc. Unfortunately, so far, the origins of the components of the received UWB signals have not been fully understood. Nevertheless, an ideal condition of accurate and contactless BP monitoring is to obtain pulse waves, since existing work [43] has established the connections between BP and pulse waves. Therefore, it is necessary to remove components of the received signals that are not related to the pulse wave, thus preventing the noise from interfering with BP prediction.

Secondly, exploiting features captured from signals is a promising way for BP prediction. Following this line, whether the extracted features are relevant to BP and whether the important features related to BP are missed becomes the key to accurate BP prediction. Previous work [27, 51, 52, 57] has focused on extracting some time-domain and frequency-domain features from the signals and adopting traditional machine learning algorithms for BP prediction. However, manual extraction of the features has its inherent weakness, that is, the design of these features mainly comes from observation of the existing data and the limited knowledge of interdisciplinary fields. These weaknesses, combined with the complex intrinsic structure and fluctuating quality of the received signals, inevitably result in the poor generalizability of these features. Therefore, there is a need for methods to automatically and effectively recognize BP-related features.

To solve the first challenge, we first capture the stationary state of a sitting subject and design multiple methods to reduce interference from noise in the 20-second signals indicating that the sitting subject is motionless. We evaluate the signals after removing interference by experiments and verify their similarity to pulse waves.

Considering that so far, no medical evidences suggest that the signal after removing interference is a pulse wave, we refer to the signals after removing interference as quasi-pulse waves.

To deal with the second challenge, we construct a deep learning model to learn BP-related features and predict BP. Deep learning provides the ability to automatically learn features from signals, thereby circumventing the limitations of manual feature extraction. In particular, the one-dimensional convolution layer has the same mathematical representation as a finite impulse response filter, rendering it suitable for processing UWB signals. Moreover, different convolution operations have demonstrated high effectiveness in capturing non-linear features. Therefore, leveraging the capacity of deep learning to discern intricate patterns and relationships within the signals, provides an efficient solution to automatically extracting BP-related features for accurate BP prediction.

To summarize, the main contributions of this paper are as follows.

- We build a BP monitoring system named RF-BP, combining biomedical signal processing and deep learning to achieve regular daily monitoring of BP using UWB signals. Specifically, RF-BP can infer BP for a sitting subject, as long as the subject is detected to be sitting still, intentionally or inadvertently, for 20 seconds.
- We propose two methods that utilize peak detection and principal component analysis (PCA) respectively to detect and remove aliased and deformed parts in the received UWB signals, after eliminating known interferences such as disturbances caused by human movements and respiration, and the reflections of static objects.
- We design a multi-scale feature extractor to extract features of quasi-pulse waves at different scales and develop an attention-augmented convolutional neural network with the bottleneck residual structure to identify the value of these features.
- We conduct extensive experiments on a self-built dataset and a public dataset. The experimental results show that our system RF-BP can accurately predict BP. Over the self-built dataset, the mean absolute error (MAE) and standard deviation (SD) for SBP are 6.5 mmHg and 6.1 mmHg, and the MAE and SD for DBP are 4.7 mmHg and 4.9 mmHg.

## 2 RELATED WORK

**BP Measurement Methods.** BP measurement methods can be broadly categorized into three main types: cuff-based methods, wearable-based methods, and contactless methods.

**Cuff-based methods.** Cuff-based BP measurement methods include auscultation and oscillometry. The mercury sphygmomanometer [48], which measures BP in conjunction with a stethoscope, was invented in 1896 by Scipione Riva-Rocci. In recent years, electronic sphygmomanometers and Holter BP device [7] using the oscillometry method have been used to measure BP [36]. While cuff-based BP measurement methods can accurately measure a user's BP, the pressure on the upper arm from the cuff can induce discomfort for the individual and the process needs assistance from others, leading to limited engagement for regular daily monitoring of BP.

**Wearable-based methods.** To enhance the convenience of BP monitoring, researchers propose to utilize wearable devices for BP monitoring. Han et al. evaluate the feasibility and stability of smartwatch-based BP monitoring in real-world conditions [21]. Rastegar et al. propose a hybrid CNN-SVR model, which could exploit feature interactions from feed-forward directions to learn more in-depth features of ECG and photoplethysmography (PPG) signals and continuously estimate SBP and DBP [44]. Sharifi et al. present a method using a multivariate adaptive regression spline, based on PTT and photoplethysmogram intensity ratio, for the continuous BP estimation [50]. Kyriacou et al. propose several SBP and DBP estimation models using recurrent neural networks with bidirectional connections and an attention mechanism utilizing only PPG signals [17]. Simjanoska et al. develop a method for BP estimation using only ECG signals, where the method combines a stacking-based classification module and a regression module for predicting SBP, DBP, and mean arterial pressure (MAP) [53]. Wen et al.

propose a noninvasive and continuous BP estimation system based on a custom-designed wearable 120 GHz Doppler radar sensor [60]. Although wearable-based methods enable BP monitoring, they all require the user to wear the additional device or affix electrodes, resulting in the inapplicability of regular daily monitoring of BP.

**Contactless methods.** To achieve contactless BP monitoring, some studies attempt to measure BP by extracting pulse wave features in a contactless manner. Jung et al. validate the feasibility of contactless BP monitoring using a 300 GHz continuous wave (CW) radar on a dataset consisting of 8 users [27]. Shi et al. present a non-contact BP measurement model based on the random forest algorithm and arterial pulse waveforms detected by a CW radar [51]. Vysotskaya et al. validate the feasibility of contactless BP monitoring using a 60GHz FMCW radar [57]. Shi et al. propose a BP measurement system leveraging the mmWave signal characteristics and features in the delay-Doppler domain [52]. Among the existing work, either the BP prediction accuracy is inadequate or the monitoring process requires a deep involvement of the user. The substandard accuracy and inconvenience associated with these methods will prevent them from effectively meeting the requirements of individuals who need regular BP measurements, such as users with fluctuating BP.

**Deep Learning for Vital Sign Monitoring.** In recent years, deep learning has been widely used in vital sign monitoring [39, 58, 61, 62]. Ravichandran et al. propose a deep learning network that adopts an encoder-decoder architecture utilizing dilated residual inception blocks to extract the respiration signal from a given PPG [45]. Khan et al. design a convolutional neural network plus a random forest estimator to classify and estimate human respiration activity using passive Wi-Fi signals [28]. Raza et al. propose a Long Short-Term Memory (LSTM) network for heartbeat sound classification [46]. Ha et al. propose a contactless seismocardiography monitoring system based on a hybrid architecture that combines signal processing with deep learning [20]. Further, RF-ECG constructs a conditional generative adversarial network to generate ECG signals from UWB signals [59]. Besides, multi-scale features and attention mechanisms have attracted a great deal of interest. The integration of multi-scale features in deep convolutional networks has been shown to enhance algorithm performance and bolster scale robustness [33, 37, 55]. The various attention mechanisms have obtained success in computer vision [15, 24, 64], natural language processing [18, 23], also including vital sign monitoring [29, 38].

Compared to these existing work, our work can accurately measure the user's BP without the need for user's deep involvement, thus enabling regular daily monitoring of BP using UWB signals in a contactless manner.

### 3 OUR SYSTEM

In this section, we first introduce the basics of blood pressure monitoring and then give the overview of our proposed BP monitoring system RF-BP.

#### 3.1 Blood Pressure Monitoring Basics

**3.1.1 Primer of UWB.** UWB is a radio technology by emitting short-duration pulses with very low power across an extremely wide frequency band. The UWB transmitter generates Gaussian pulses  $g(t)$  modulated on a carrier frequency  $f_c$ . The transmitted signal  $x(t)$  can be represented as:

$$x(t) = g(t) \cdot \cos(2\pi f_c t) \quad (1)$$

The transmitted signals will be reflected off subjects in the environment and returned to the UWB device. By conducting channel estimation, the receiver obtains the channel impulse response. The pulse signals can be reflected from objects at different distances. So, the received signals can be represented as:

$$b(t) = \sum_{p=1}^P \alpha_p x(t - t_p) \quad (2)$$

where  $p$  is the number of paths,  $\alpha_p$  is the reflection coefficient,  $t_p$  is the time delay.

By calculating the distance between the target and the UWB device, the required signals can be obtained, which can be represented as:

$$\hat{b}(t) = \alpha_p x(t - t_p) \quad (3)$$

$$t_p = \frac{2d}{c} \quad (4)$$

where  $c$  is the signal propagation speed of light in the vacuum and  $d$  is the tiny change in distance between the target and the UWB device.

**3.1.2 Principle of PTT-based Blood Pressure Measurement.** The pulse waves are formed by the blood transmitted from the heart to the systemic circulatory system through the arteries during cardiac contraction. The BP can be estimated by extracting features from pulse waves. PTT, i.e., the time of a pulse wave traveling between two arterial sites, is considered the most reliable and well-accepted feature to estimate BP. In the following, we will introduce the principle of PTT-based BP measurement.

First, the Moens-Korteweg equation [31] characterizes PWV in terms of the incremental elastic modulus  $E$  of the vessel wall, the wall thickness  $h$ , the radius  $r$  and the blood density  $\rho$ , denoted as:

$$PWV = \sqrt{\frac{Eh}{2r\rho}} \quad (5)$$

where it assumes that there is little or no change in vessel area, wall thickness and density.

Hughes et al. find that the elastic modulus of the vessel wall increases exponentially with mean arterial pressure (MAP) [25], which is expressed as:

$$E = E_0 e^{\beta MAP} \quad (6)$$

where  $E_0$  is the elastic modulus at zero blood pressure,  $\beta$  is a material coefficient of the artery,  $MAP = \frac{1}{3}SBP + \frac{2}{3}DBP$ .

Let  $PTT_0$  and  $MAP_0$  be the average values of PTT and MAP, we can obtain:

$$MAP = MAP_0 + \frac{2}{\beta} \ln\left(\frac{PTT_0}{PTT}\right) \quad (7)$$

Then, the Bramwell-Hill equation [14] provides the relationship between arterial distensibility and PWV, expressed as:

$$PWV = \sqrt{\frac{V \cdot \Delta P}{\rho \cdot \Delta V}} \quad (8)$$

where  $V$  is the volume per unit length and  $P$  is the pressure.

In the arterial system, changes in pressure can be considered as changes in BP, i.e. pulse pressure (PP),  $\Delta P = PP = SBP - DBP$ . Let  $PP_0$  be the average value of  $PP$ , we can obtain:

$$PP = PP_0 \times \left(\frac{PTT_0}{PTT}\right)^2 \quad (9)$$

Finally, solving the simultaneous equations consisting of Equation 7 and Equation 9, SBP and DBP can be represented as:

$$DBP = \frac{1}{3}SBP_0 + \frac{2}{3}DBP_0 + \frac{2}{\beta} \ln\left(\frac{PTT_0}{PTT}\right) - \frac{SBP_0 - DBP_0}{3} \times \left(\frac{PTT_0}{PTT}\right)^2 \quad (10)$$

$$SBP = DBP + (SBP_0 - DBP_0) \times \left(\frac{PTT_0}{PTT}\right)^2 \quad (11)$$

### 3.2 Overview of Our System

RF-BP consists of three modules: human presence and state identification, quasi-pulse wave extraction, and blood pressure estimation. Figure 2 shows the architecture of RF-BP.

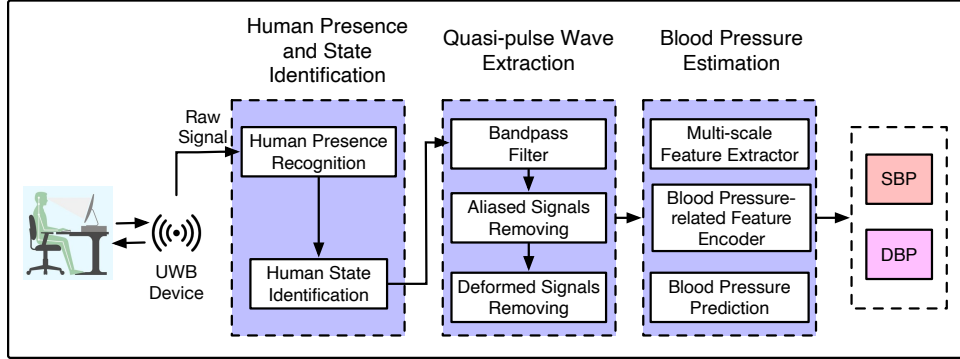


Fig. 2. System architecture.

**Human presence and state identification.** This module consists of two components, namely, human presence recognition and human state identification. Given the received signals, we first apply the background subtraction to remove the clutter caused by static reflection in the environment, obtaining the accurate channel impulse response (CIR). Then, by detecting the peak of the CIR and analyzing the distance between the user and the device, we can identify whether the user is present. Finally, we indirectly infer whether the user is in a continuous stationary state based on the periodicity of the user’s respiration waveform. If the user is found to be present and in a continuous stationary state, then the quasi-pulse wave will be extracted to predict BP.

**Quasi-pulse wave extraction.** Given the signals output by the previous module, we first apply a filter to obtain pseudo pulse waves. Then, for removing aliased and deformed pulse waves, we adopt Automatic Multiscale-based Peak Detection (AMPD) algorithm to locate the peaks of each pulse in the pseudo pulse waves, and propose two methods that utilize peak detection and PCA to identify aliased and deformed parts in pseudo pulse waves, respectively.

**Blood pressure estimation.** To accurately estimate BP using quasi-pulse waves, we construct a deep learning model. Considering that the BP pulse has similarities with the blood volume pulse [13], we refer to the processing of PPG reflecting blood volume changes [54], and take the quasi-pulse waves and their first-order derivatives as the input of the model to extract BP-related features from different dimensions. Further, we take the convolution operation as the backbone operation and incorporate residual connections, a multi-scale feature extractor and a channel attention mechanism to form a lightweight and effective model.

### 3.3 Human Presence and State Identification

To monitor BP, the RF-BP needs to identify from the received signals whether the user is present and in a continuous stationary state.

The received signals mainly comprise reflection of the human body and static objects within the environment. However, the presence of reflection of the static objects significantly affects the estimation of CIR in the received signals. Therefore, we apply the dynamic background subtraction method to remove the clutter caused by static reflection in the environment, retaining the signals reflected off the human body. In principle, when a user is within the sensing range, the peak of the CIR amplitude is large, and the distance between the user and the device

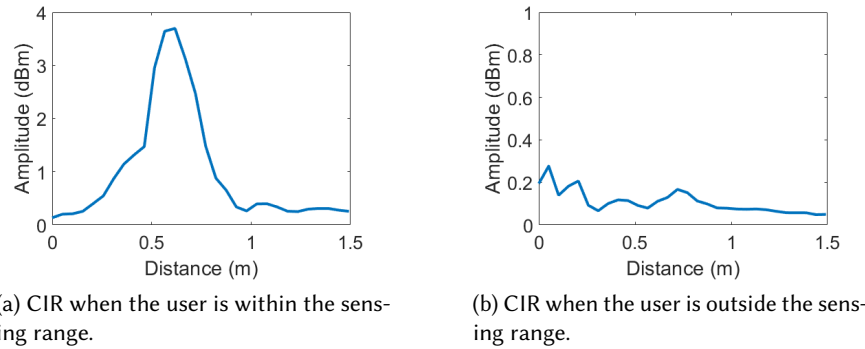


Fig. 3. CIRs of received signals.

can be obtained from the peak position of the CIR. When a user is outside the sensing range, the peak of the CIR amplitude is small, and the distance between the location corresponding to the peak position and the device is close, typically within 20cm. Therefore, we can identify whether the user is present by analyzing the amplitude and location of the CIR peak. Figure 3 gives examples of the CIR of received signals when the user is within and outside the sensing range.

After obtaining the distance between the user and the device, the signal phase corresponding to that distance can be extracted and treated as the vital sign signal. However, even when the user is present, for the delicate task of BP monitoring, slight body movements of the user will overwhelm the pulse wave in the received UWB signal, ultimately rendering it difficult to measure BP accurately. Therefore, we need to design a method to identify whether the user is in a stationary state.

As we know, when a user is in a continuous stationary state, the respiration signal will dominate the obtained signal phase and the autocorrelation coefficient of the signal phase will be larger. Therefore, we calculate the periodicity of the signal phase by the autocorrelation function and then infer whether the user is in a continuous stationary state. Specifically, when the autocorrelation coefficient is greater than 0.6, the user is considered to be in a continuous stationary state, otherwise, the user is considered to be in a body-movement state. Figure 4

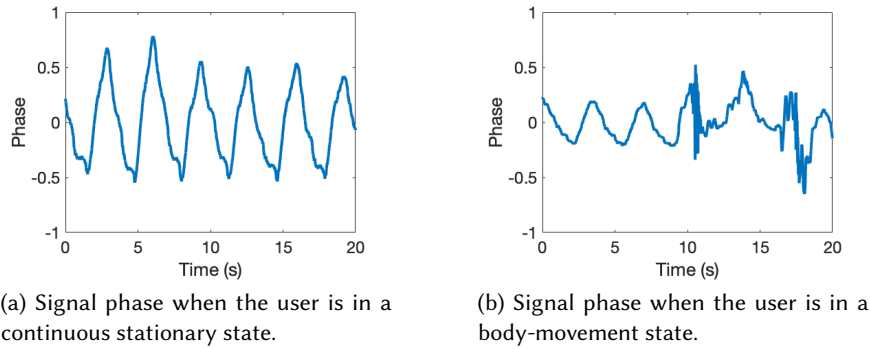


Fig. 4. Phase of received signals.

gives two examples. In Figure 4a, the autocorrelation coefficient of the signal phase is 0.81 when the user is in a continuous stationary state. In Figure 4b, the autocorrelation coefficient of the signal phase is 0.32 when the user is in a body-movement state.

We divide the signal into segments of 20s duration for human state identification. The choice of a 20s duration is based on the consideration that it is easier for the user to remain stationary for this duration. Additionally, the breaths contained within the 20s signal are sufficient to identify the user's state.

Then, we discard the segments in the body-movement state and the segments in the stationary state are used to extract the quasi-pulse waves and estimate the BP.

### 3.4 Quasi-pulse Wave Extraction

To extract the quasi-pulse waves from the signal phases, we apply a second-order Butterworth zero-phase-shift filter to eliminate interferences, such as respiration, from the signal phases. Considering that the main frequency of the pulse waves is between 0.8Hz and 10Hz [40], we set the bandpass frequency range from 0.8Hz to 10Hz.

The wave that passes through the filter is called the pseudo pulse wave because we observe that most filtered waves exhibit characteristics of vascular contraction and diastole, but some have aliased or deformed parts. The existence of these anomalous parts can potentially compromise the accuracy of BP estimation. Therefore, we design the following methods to identify the aliased and deformed parts from the pseudo pulse waves.

First, we adopt the AMPD algorithm to locate the peaks of each pulse in the pseudo pulse waves. Figure 5 gives an example where the marked points (in all colors) are the peaks of the pulses identified by the AMPD algorithm. The algorithm of AMPD is shown in Algorithm 1.

Next, for identifying aliased parts from a pseudo pulse wave, we adopt the Fast Fourier Transform (FFT) to calculate the user's pulse rate  $f_R$  and get the average samples between two pulses by  $\frac{f_s}{f_R}$ , where  $f_s$  is the sampling rate of the pulse wave. We calculate the difference between  $\frac{f_s}{f_R}$  and the intervals of peak locations of each pulse detected by AMPD. If the difference exceeds the preset threshold, an aliased peak is identified. In Figure 5, the green point is an identified aliased peak.

Then, we propose a PCA-based method to identify the deformed parts in pseudo pulse waves. Specifically, we consider a signal segment with a length of  $\frac{f_s}{f_R}$ . This signal segment is treated as a representation of a single pulse. By collecting the signals of all the pulses, we form a matrix where each row corresponds to a pulse. Subsequently, we apply PCA to this matrix. PCA enables us to extract the principal components of the pulses, which capture the main patterns or variations within the pulses. The basic process of the algorithm is as follows. First, it calculates the covariance matrix of the pulse matrix, then calculates the eigenvalues and eigenvectors of the covariance matrix, keeps the eigenvector corresponding to the largest eigenvalue, and multiplies this eigenvector with the

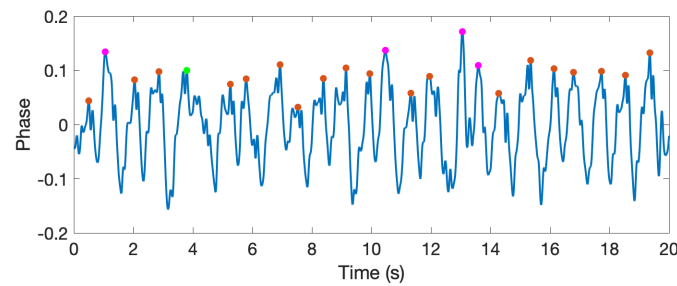


Fig. 5. Peaks in pseudo pulse waveform.

**Algorithm 1:** Automatic Multiscale-based Peak Detection.

**Input:** The pseudo pulse wave  $R$  with a duration of 20s.

**Output:** Peak locations  $\mathbf{p}$  of each pulse.

- 1 Decompose the pseudo pulse wave  $R$  into subsequences of length  $2k + 1$ ,  $k = 1 \sim \frac{l}{2} - 1$ , respectively, with  $l$  being the length of  $R$ .
- 2 Let  $\mathbf{LP}_{m \times n}$  store the local minima of each subsequence, where  $m = \frac{l}{2} - 1$ ,  $n = l$ . All values in  $\mathbf{LP}$  are initialized to 0.
- 3 For each subsequence, calculate the location of its local minima and set the corresponding value in  $\mathbf{LP}$  to 1.
- 4 For each scale of subsequence, calculate the cost function  $G$ ,  $G(i) = \sum_{j=1}^l \mathbf{LP}(i, j)$ ,  $i = 1 \sim m$ .
- 5 Determine a threshold based on  $G$ , i.e., obtain the index of the maximum value of  $G$ , denoted  $k_s$ .
- 6 Select the peak  $p_i$  that satisfies  $\mathbf{LP}(k, p_i) = 1$ ,  $k = 1 \sim k_s$ , as the detected peak. The locations of all detected peaks are denoted as  $\mathbf{p} = \{p_i\}$ .

original pulse matrix to get the principal component of the pulses. Finally, it calculates the cosine similarity between the principal component of the pulse and each row of the pulse matrix. If the similarity is less than 0.8, a deformed peak is identified. In Figure 5, the purple points are the identified deformed peaks.

For each peak except for those identified as aliased or deformed, we take the first 4s and the last 4s of the signal centered on this peak and form a quasi-pulse wave. These quasi-pulse waves will be used for subsequent BP estimation.

The algorithm for quasi-pulse wave extraction described in this section is shown in Algorithm 2.

We validate that the quasi-pulse waves are highly similar to the output of pulse wave detection devices in shape. Specifically, we use the HK-2000C [6], a digital pulse sensor, as the ground truth device. The HK-2000C obtains

**Algorithm 2:** Quasi-pulse Wave Extraction.

**Input:** The pseudo pulse wave  $R$  with a duration of 20s.

**Output:** Quasi-pulses  $\mathbf{R}_p$ .

- 1 Apply AMPD algorithm to obtain the peak locations  $\mathbf{p}$  of each pulse.
- 2 Apply FFT to obtain the pulse rate  $f_R$ , the signal length of a pulse can be calculated by  $l_R = \frac{f_s}{f_R}$ .
- 3 Let  $n_p$  be the length of  $\mathbf{p}$ , threshold is set to identify aliased pulses.
- 4 **for**  $i \leftarrow 0$  **to**  $n_p - 1$  **do**
- 5     **if**  $|p_{i+1} - p_i - l_R| > threshold$  **then**
- 6         mark  $p_i$  as an aliased peak
- 7     **end**
- 8 **end**
- 9 Let  $\mathbf{R}'(i)$  be  $\{R_j\}_{j=p_i-\frac{l_R}{2}}^{p_i+\frac{l_R}{2}}$ .
- 10 Find the eigenvectors  $\mathbf{W}$  and eigenvalues  $\mathbf{ev}$  of  $\mathbf{R}' = \{\mathbf{R}'(i)\}_{i=1}^{n_p}$ .
- 11 Obtain the index of the maximum value of  $\mathbf{ev}$ , denoted  $max_p$ .
- 12 Obtain the principal component of the pulses,  $R_{pca} = \mathbf{R}' \times \mathbf{W}_{max_p}$ .
- 13 Calculate the cosine similarity between  $R_{pca}$  and each row of  $\mathbf{R}'$ , mark the peaks of pulses with similarity less than 0.8 as the deformed peaks.
- 14 Take the first 4s and the last 4s of  $R$  centered on the unmarked peaks and form quasi-pulse waves  $\mathbf{R}_p$ .

pulse waves by strapping it to the chest. Figure 6 shows the waves obtained from the HK-2000C and quasi-pulse waves output by quasi-pulse wave extraction module simultaneously. It can be seen that the quasi-pulse wave is almost identical to the ground truth, and their Pearson Correlation Coefficient (PCC) is 0.93.

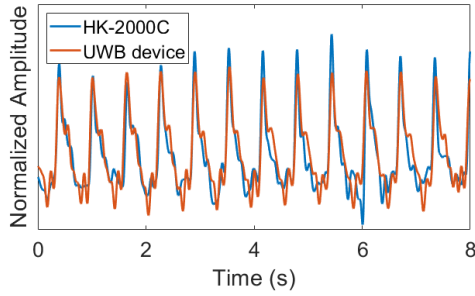


Fig. 6. Pulse waves obtained from the HK-2000C and quasi-pulse waves in RF-BP, respectively.

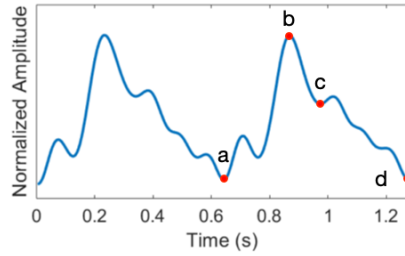


Fig. 7. Blood pressure related features in a quasi-pulse wave.

Further, we analyze a quasi-pulse wave carefully and find that the wave exhibits characteristics of vascular contraction and diastole. As shown in Figure 7, point *a* corresponds to the moment of minimum arterial volume, when the heart contracts and ejects blood rapidly. Point *b* corresponds to the moment of maximum arterial volume, i.e., the end of the rapid ejection, after which arterial volume decreases due to the decrease in ejection rate. Point *c* denotes the beginning of diastole. Point *d* indicates the beginning of the next cardiac cycle.

As depicted in Figure 6 and Figure 7, the quasi-pulse waves exhibit characteristics of vascular contraction and diastole. Accordingly, we can utilize these waves to extract BP-related features and then estimate BP.

### 3.5 Blood Pressure Estimation

After extracting the quasi-pulse waves, we need to extract useful features for BP prediction. Therefore, we construct a deep learning model to automatically learn features from the quasi-pulse waves and predict BP. The model takes the quasi-pulse wave  $R_p$  and its first-order derivative  $R'_p$  as input, and outputs SBP and DBP. The model has the architecture as shown in Figure 8, containing three components: a multi-scale feature extractor, a BP-related feature encoder, and a prediction layer, where the BP-related feature encoder consists of multiple attention-augmented residual blocks, and  $C$  is the number of channels.

In the task of BP estimation, users with different BP exhibit distinct BP-related features. Therefore, employing a fixed-scale convolution kernel would overlook certain BP-related features. To address this limitation, we design

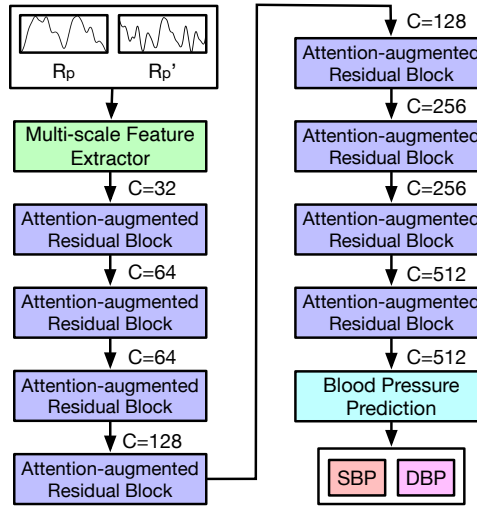


Fig. 8. The architecture of the model.

a Multi-scale Feature Extractor (MFE) to extract features of pulse waves at different scales, enabling the model to capture the rich and deep features from the pulse waves.

As shown in Figure 9, the multi-scale feature extractor consists of four feature extraction blocks, each of which has the same structure except for the size of the convolution kernel, which is 5, 9, 13, or 17, respectively. The feature extraction block contains a 1D convolutional layer, a batch normalization layer, and ReLU as the activation function. And the number of output channels of each feature extraction block is 8. To maintain the same output size, padding is applied in each convolutional layer. The features extracted from each feature extraction block at different scales are concatenated to form the final feature representation. The feature map, i.e., output of

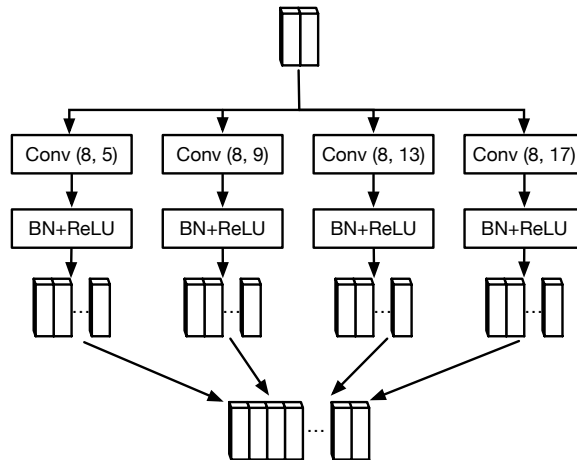


Fig. 9. The structure of the multi-scale feature extractor.

the multi-scale feature extractor, contains features at multiple scales, thereby enhancing the accuracy of BP estimation, particularly for hypertensive users.

Furthermore, different channels of the feature map may have varying degrees of effect on BP. To improve the accuracy of BP estimation, we propose a channel attention mechanism and integrate it with the residual block, forming the attention-augmented residual block. The channel attention mechanism enables the residual block to focus on the BP-related features while suppressing those that are not.

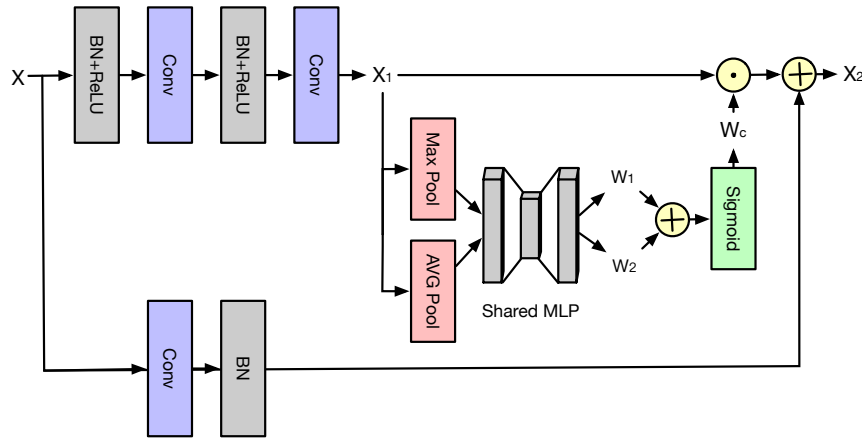


Fig. 10. The structure of the attention-augmented residual block.

The attention-augmented residual block, whose structure is shown in Figure 10, mainly consists of the residual connection and channel attention (CA). The input of the attention-augmented residual block is the feature map  $X \in \mathbb{R}^{C \times L}$ , where  $C$  is the number of channels and  $L$  is the length of features. The feature map  $X$  is first passed through two convolutional layers to obtain the feature map  $X_1$ . Then, both average-pooling and max-pooling operations are employed to aggregate spatial information of the feature map  $X_1$ , generating two different spatial context descriptors:  $X_{avg}^c$  and  $X_{max}^c$ , which denote average-pooled features and max-pooled features, respectively. To derive the channel attention map  $W_c \in \mathbb{R}^{C \times 1}$ , both descriptors are forwarded to a shared Multi-Layer Perceptron (MLP). The shared MLP produces weights  $w_1$  and  $w_2$ .  $w_1$  and  $w_2$  are then summed up and passed through a sigmoid activation function, yielding the channel attention map  $W_c$ . The channel attention map represents the weights assigned to each channel, ranging between 0 and 1. Finally, the Hadamard product of  $W_c$  and  $X_1$  is computed to obtain the enhanced feature representation  $X_a$ . The process can be expressed as:

$$W_c = \sigma(MLP(X_{avg}^c) + MLP(X_{max}^c)) \quad (12)$$

$$X_a = X_1 \odot W_c \quad (13)$$

We adopt the bottleneck residual block that utilizes a  $1 \times 1$  convolution layer to create a bottleneck. Ultimately, the process of attention-augmented residual block can be represented as:

$$X_2 = BN(Conv(X)) + X_a \quad (14)$$

Finally, the extracted BP-related features are used to predict BP through a prediction layer consisting of an AVG pooling and a fully connected layer, obtaining the SBP and BDP.

We adopt Huber loss as the loss function of the model. The Huber loss is basically the absolute error but becomes the squared error when the absolute error is small, so it offers advantages over the squared error loss by being insensitive to outliers in the input while maintaining differentiability. It is represented as:

$$L_{\text{Huber}}(y, \tilde{y}) = \begin{cases} \frac{1}{2}(y - \tilde{y})^2, & \text{for } |y - \tilde{y}| < \delta \\ \delta|y - \tilde{y}| - \frac{1}{2}\delta^2, & \text{otherwise} \end{cases} \quad (15)$$

where  $y$  and  $\tilde{y}$  are the ground truth and predicted BP, respectively, and  $\delta$  is a hyperparameter, which takes the default value of 1.

Since SBP is more difficult to predict than DBP, i.e., the predicted error of SBP is larger in general, we design a weighted loss function as the final loss function, denoted as:

$$L = \lambda L_{\text{Huber}}^{\text{SBP}} + L_{\text{Huber}}^{\text{DBP}} \quad (16)$$

where  $\lambda$  ( $\lambda > 1$ ) is a hyperparameter.

## 4 EXPERIMENTAL EVALUATION

### 4.1 Experimental Setup

**4.1.1 Hardware.** We use a commercial sensor, i.e., X4M05, to transmit and collect UWB signals. The sensor has the center frequency of 7.3GHz and the bandwidth of 1.4GHz. We set the frames per second (FPS) to 200, which is enough to extract pulse waves and predict BP. The sensor is connected to a Raspberry Pi, which controls the transmitting and receiving of UWB signals. All of them are packaged into a compact device whose appearance and internal structure are shown in Figure 11.

We adopt Omron HEM-7132 [9], an FDA-approved sphygmomanometer with an arm cuff as shown in Figure 12, to measure BP, whose values are treated as the ground truths.

**4.1.2 Software.** Our system is implemented in Matlab R2022a, Python 3.6 and PyTorch 1.11.0. Human presence and state identification, quasi-pulse wave extraction modules are implemented using Matlab. The extracted quasi-pulse waves are fed into the deep learning model implemented in Python to predict BP. During the training phase, we adopt the Adam optimizer. We set the initial learning rate to 0.001, and adopt a learning rate decay strategy. Specifically, the learning rate for parameters is decayed by a factor of 0.8 every 5 epochs. The value of  $\delta$  is searched within the set {1, 5, 10, 15, 20} and finally set to 15. The value of  $\lambda$  is searched within the set {1.2, 1.5, 1.8} and finally set to 1.5. The batch size is set to 32. Training will stop when the loss on the validation set is no longer decreasing.



Fig. 11. Our device.



Fig. 12. Ground truth device.



Fig. 13. Experimental scenario.

**4.1.3 Practical Deployment.** Our UWB module is packaged in a 3D printed box, requiring only a connection to a power source for operation. In real-world scenarios, the user places the device on the desk, orienting it towards the person, and connects it to a power source. Subsequently, the device automatically receives data and predicts BP.

**4.1.4 Datasets.** To evaluate the performance of RF-BP, we recruit 70 participants including 40 females and 30 males in the age range of 25 - 80 for the experiments. Among them, 13 subjects have been diagnosed with hypertension. Before the experiments, each participant is informed about the measurements. We have obtained written consent from all participants, and our Institutional Review Boards have approved entire research activities.

We conduct our experiments in a typical office environment, as shown in Figure 13, where the UWB device is placed on the desk and the participant sits at the desk, 30-60cm away from the device. The ground truth is measured simultaneously by the Omron HEM-7132. Each data collection lasts approximately 40 seconds. Ultimately, we collect 60-hour signal data. The distribution of BP corresponding to our collected signal data is shown in Figure 14.

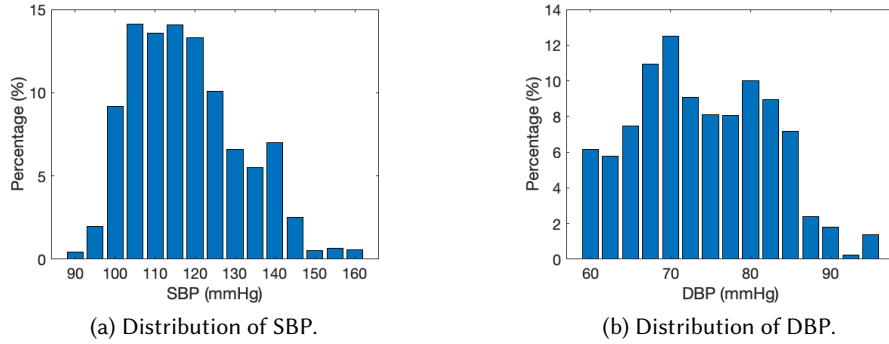


Fig. 14. Distribution of blood pressure in our collected data.

In addition, we use a public dataset [49] which is published by Nature Research, hereafter referred to as the Nature dataset, to evaluate RF-BP. The Nature dataset contains clinically recorded radar vital signs with synchronized BP. 30 subjects are measured in the Nature dataset. The Nature dataset contains about 12,000 BP measurements. The distribution of BP corresponding to nature dataset is shown in Figure 15.

To evaluate the performance of our system, we perform the k-fold cross-validation on each dataset. That is, the dataset is divided equally into  $k$  groups according to the number of subjects and the following procedure is repeated  $k$  times. Each time, a group is selected as the test set, one of the remaining groups is used as the validation set and the other  $k - 2$  groups are put together to form the training set. Note that adopting the k-fold cross-validation strategy for partitioning the dataset ensures that the subjects in the test set are distinct from those in the training set. Consequently, the trained model can be applied by any individual in real-world scenarios.

**4.1.5 Metrics.** We employ mean error (ME), mean absolute error (MAE) and standard deviation (SD) to evaluate the performance of RF-BP.

$$ME = \frac{1}{N} \sum_{i=1}^N (y_i - \tilde{y}_i) \quad (17)$$

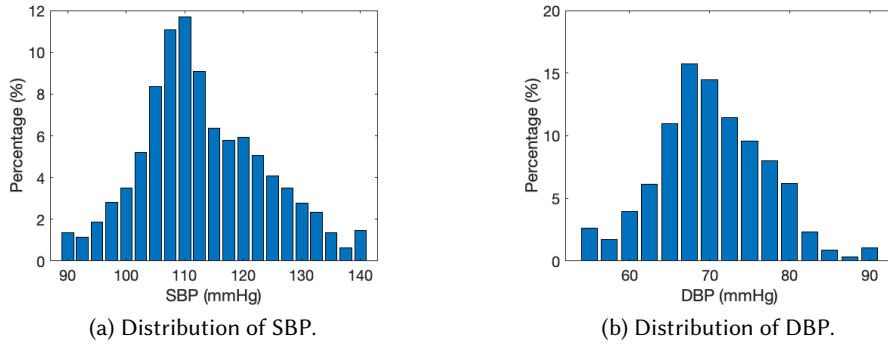


Fig. 15. Distribution of blood pressure in the Nature dataset.

$$MAE = \frac{1}{N} \sum_{i=1}^N |y_i - \tilde{y}_i| \quad (18)$$

$$SD = \sqrt{\frac{1}{N-1} \sum_{i=1}^N (y_i - \tilde{y}_i)^2} \quad (19)$$

where  $N$  is the number of samples,  $y_i$  and  $\tilde{y}_i$  are the ground truth and estimated BP, respectively.

In addition, we employ the international standard to evaluate the performance of RF-BP. The Association for the Advancement of Medical Instrumentation (AAMI) has established an error standard for BP, i.e., SP10 [1]. According to AAMI SP10, the ME of predicted SBP and DBP should be less than  $\pm 5$  mmHg, and the SD should be less than 8 mmHg. However, since the ME and SD are susceptible to outliers, the British Hypertension Society (BHS) has devised more stringent criteria, considering the percentages of absolute errors within 5, 10 and 15 mmHg [42]. The BHS criteria are shown in Table 1.

Table 1. British hypertension society grading criteria

Grade	Absolute error between standard and test device		
	$\leq 5$ mmHg	$\leq 10$ mmHg	$\leq 15$ mmHg
A	60%	85%	95%
B	50%	75%	90%
C	40%	65%	85%
D	Worse than C		

## 4.2 Performance Analysis

We calculate MEs, MAEs, SDs according to the estimated values RF-BP outputs and the ground truth, and then grade the results according to AAMI SP10 standard and BHS criteria, respectively.

On the RF-BP dataset, the ME, MAE, and SD of SBP are 0.7 mmHg, 6.5 mmHg and 6.1 mmHg, respectively. And the ME, MAE, and SD of DBP are 0.2 mmHg, 4.7 mmHg and 4.9 mmHg, respectively. These results indicate that the predictions for SBP and DBP meet the AAMI SP10 standard. Furthermore, for SBP, the percentages of absolute errors within 5, 10, and 15 mmHg are reported as 52.0%, 78.4% and 95.2%, respectively. Similarly, for DBP,

Table 2. System performance according to BHS criteria

		$\leq 5 \text{ mmHg}$	$\leq 10 \text{ mmHg}$	$\leq 15 \text{ mmHg}$	Grade
RF-BP dataset	SBP	52.0%	78.4%	95.2%	B
	DBP	62.1%	89.8%	99.1%	A
Nature dataset	SBP	55.1%	84.9%	98.0%	B
	DBP	66.8%	93.5%	99.2%	A

the percentages of absolute errors within these thresholds are found to be 62.1%, 89.8% and 99.1%. According to the BHS criteria, SBP predictions achieve a rating of grade B and DBP predictions reach grade A, as shown in the upper part of Table 2.

On the Nature dataset, the ME, MAE, and SD of SBP are 0.9 mmHg, 5.5 mmHg and 5.3 mmHg, respectively. And the ME, MAE, and SD of DBP are 0.2 mmHg, 4.1 mmHg and 4.3 mmHg, respectively. These results indicate that both the predicted SBP and DBP values meet the AAMI SP10 standard. Furthermore, for SBP, the percentages of absolute errors within 5, 10, and 15 mmHg are reported as 55.1%, 84.9% and 98.0%, respectively. Similarly, for DBP, the percentages of absolute errors within these thresholds are found to be 66.8%, 93.5% and 99.2%. According to the BHS criteria, SBP predictions achieve a grade B rating and DBP predictions reach grade A, as shown in the lower part of Table 2.

Comparing the experimental results on these two datasets, the BP estimation performance on Nature dataset outperformed that on RF-BP dataset. It should be mentioned that the Nature dataset is collected with the subjects lying flat on the bed and their upper bodies facing the radar. In our experiments, the participant sits at the desk. Therefore, the radar signals in the Nature dataset have a greater SNR, thus leading to a better performance.

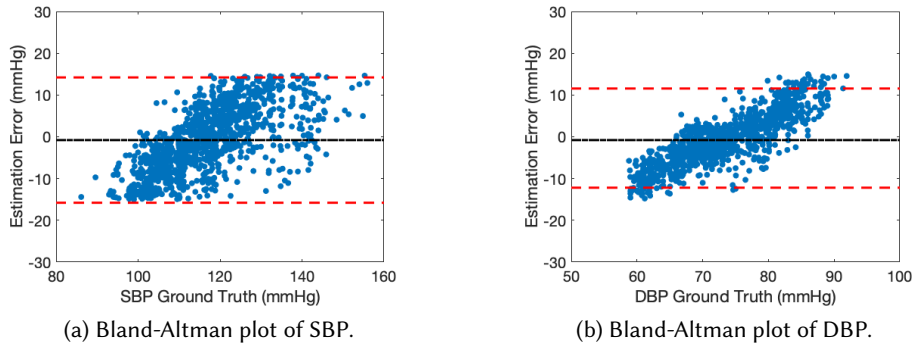


Fig. 16. Bland-Altman plots of blood pressure on RF-BP dataset.

Bland-Altman plots are often used to evaluate the agreement between two measurements techniques. If most of the points fall within the limits of agreement ( $ME \pm 1.96 \times SD$ ), they are considered to be in good agreement. As shown in Figure 16 and Figure 17, we plot the Bland-Altman plots of SBP and DBP on the RF-BP dataset and the Nature dataset, respectively, where the black dot dash line represents the ME and the red dash line represents the limits of agreement. Most of the points (i.e., more than 94% points) fall within the limits of agreement, which indicates that the BP predicted by RF-BP is in good agreement with the BP measured by the ground truth device.

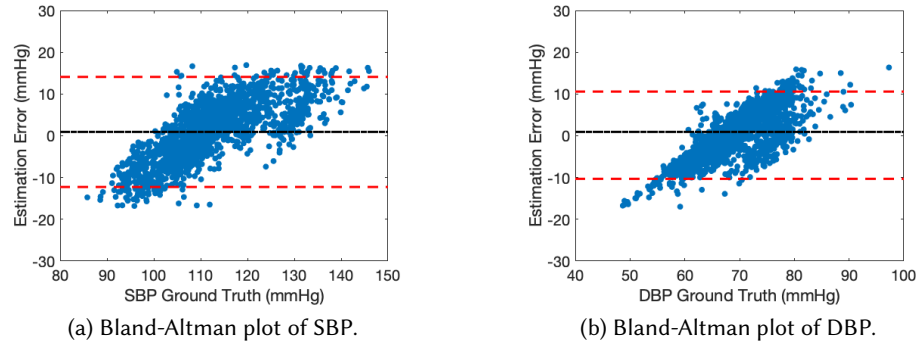


Fig. 17. Bland-Altman plots of blood pressure on Nature dataset.

To summarize, the accuracy of RF-BP meets the AAMI SP10 standard, and reaches grade B for SBP and grade A for DBP in terms of the BHS criteria. In addition, BP predicted by RF-BP has good agreement with the ground truth. This indicates that RF-BP is competent for the task of daily BP monitoring.

#### 4.3 Comparison to Existing Work

To provide a comprehensive evaluation of RF-BP, we compare its performance to that of previous work focusing on contactless BP measurement [27, 51, 57]. We perform signal processing on our dataset to obtain the pulse waves, reproduce the feature extraction of previous work and adopt the corresponding machine learning algorithms for BP prediction, respectively. Table 3 lists the performance of our work and three existing methods. The second row lists the performance of RF-BP on the RF-BP dataset, while the third through fifth rows give the performance of previous work. It can be seen that RF-BP exhibits the best performance in terms of BP estimation compared to the three existing methods.

Table 3. System performance compared to existing work, MRE represents mean relative error.

	SBP-MAE	DBP-MAE	SBP-SD	DBP-SD	SBP-MRE	DBP-MRE
RF-BP	6.5	4.7	6.1	4.9	5.6%	6.4%
[51]	7.8	6.5	7.2	6.1	6.3%	7.9%
[27]	8.1	6.3	7.6	6.0	6.7%	7.7%
[57]	7.6	6.2	6.7	5.9	6.2%	7.7%

In addition, since the SBP predicted by [52] is all within the normal BP range, for fairness, we evaluate the performance of RF-BP for users with normal SBP on the RF-BP dataset, the results are shown in Table 4. Both SBP and DBP estimated by RF-BP meet the AAMI SP10 standard. For SBP, the absolute percentages of errors within 5, 10, and 15 mmHg are reported as 68.0%, 90.8% and 99.1%, respectively. For DBP, the percentages of absolute errors within these thresholds are found to be 74.6%, 97.5% and 100%. According to the BHS criteria, both SBP and DBP predictions reach a grade A rating. It can be seen that when predicting the BP for users with normal SBP, the accuracy of RF-BP is higher than that reported by [52].

Table 4. System performance for users with normal blood pressure.

	SBP-ME	DBP-ME	SBP-SD	DBP-SD
RF-BP	0.52	0.35	4.94	4.32
[52]	0.87	1.55	5.01	5.27

#### 4.4 Ablation Study

In this paper, we propose following improvements to increase the accuracy of BP estimation: designing a multi-scale feature extractor (i.e., MFE) to extract features from multiple scales of the pulse waves, proposing the integration of a channel attention mechanism with the residual block (i.e., CA), forming the attention-augmented residual block. To evaluate the effectiveness of these proposed improvements, we conduct an ablation study and the experimental results are shown in Table 5.

Table 5. Results of ablation study.

Method	MAE		SD		AAMI		BHS	
	SBP	DBP	SBP	DBP	SBP	DBP	SBP	DBP
RF-BP	6.5	4.7	6.1	4.9	✓	✓	B	A
RF-BP - MFE	7.4	5.3	6.5	5.0	✓	✓	C	A
RF-BP - CA	7.9	5.8	6.9	5.4	✓	✓	C	A

As shown in Table 5, the MAEs of SBP and DBP predicted by RF-BP are 6.5 mmHg and 4.7 mmHg, respectively, while the SDs are 6.1 mmHg and 4.9 mmHg, respectively, which meet the AAMI SP10 standard. Moreover, SBP predictions reach a grade B rating and DBP predictions reach a grade A rating in terms of the BHS criteria.

Upon removing MFE, the MAEs of SBP and DBP increase by 0.9 mmHg and 0.6 mmHg, respectively, while the SDs of SBP and DBP increase by 0.4 mmHg and 0.1 mmHg, respectively. Upon removing CA, the MAEs of SBP and DBP increase by 1.4 mmHg and 1.1 mmHg, respectively, while the SDs of SBP and DBP increase by 0.8 mmHg and 0.5 mmHg, respectively.

Table 6. Performance of ablation study according to BHS criteria.

Method		$\leq 5$ mmHg	$\leq 10$ mmHg	$\leq 15$ mmHg	Grade
RF-BP	SBP	52.0%	78.4%	95.2%	B
	DBP	62.1%	89.8%	99.1%	A
RF-BP - MFE	SBP	46.4%	75.8%	94.7%	C
	DBP	60.2%	87.2%	97.9%	A
RF-BP - CA	SBP	46.2%	74.2%	94.6%	C
	DBP	60.0%	86.2%	97.8%	A

In addition, we detail the effect of each improvement according to the BHS grading criteria, as shown in Table 6. Upon removing MFE, the percentages of absolute errors for SBP within 5 and 10 mmHg are reduced by 5.6% and 2.6%, and the percentages of absolute errors for DBP within 5 and 10 mmHg are reduced by 1.9% and 2.6%. Upon removing CA, the percentages of absolute errors for SBP within 5 and 10 mmHg are reduced by 5.8% and 4.2%, and the percentages of absolute errors for DBP within 5 and 10 mmHg are reduced by 2.1% and 3.6%. The changes in the percentages of absolute errors within 15 mmHg for both SBP and DBP are less significant.

These results demonstrate that the proposed improvements contribute to minimizing errors and reducing variability, leading to more accurate and reliable BP estimation.

#### 4.5 Robustness Analysis

**4.5.1 Regular daily monitoring of BP.** To demonstrate the performance of RF-BP in real-world scenarios, we conduct a 30-minute experiment with the UWB device placed at a desk. In the first 5 minutes, no one is within the sensing range, and then the user is required to sit down at the desk and start working but not required to sit still. After working 20 minutes, the user leaves. Figure 18 shows the user states and blood pressure monitored by RF-BP, where states 1, 2, and 3 indicate that there is no one within the sensing range, the user is in a body-movement state and the user is in a continuous stationary state, respectively. From Figure 18, we find that RF-BP can identify that the user is in state 3 at the 12th minute and the 20th to 25th minute and accurately predicate BP for the user in state 3. This demonstrates that RF-BP can help a user obtain BP effortlessly, making daily monitoring of BP no longer a burden.

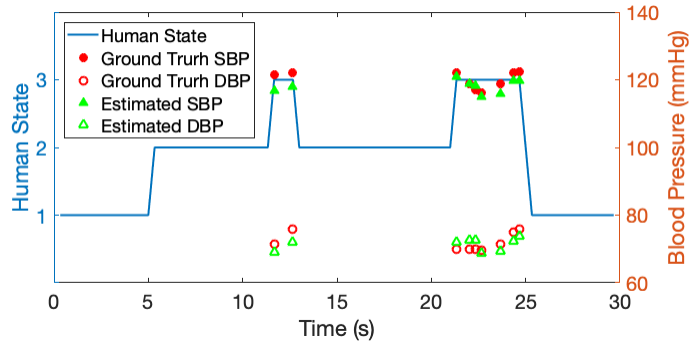


Fig. 18. Regular daily monitoring of BP.

**4.5.2 The Impact of User-device Distance.** We evaluate the performance of our system when users are located at various distances away from the device. We vary the distance between the device and the participant from 0.1 m to 3.1 m at a step size of 0.3 m. Figure 19 shows the estimated errors under different distances. It can be seen that when the distance increases, the MAEs of the SBP and DBP predictions decrease, reach the minimum errors at 0.4 m, and then the errors increase again as the distance continues to increase. In the range of 0.1 m to 1.6 m, the MAEs of SBP and DBP predictions are small enough to meet the requirements of regular daily monitoring of BP. However, when the user-device distance is 0.1 m or less, the strong direct signal may lead to inaccuracies in BP prediction. When the user-device distance exceeds 1.6 m, the MAEs of SBP and DBP predictions are too large to be used for regular daily monitoring of BP. We also demonstrate the impact of user-device distance on the received signal strength (RSS). Figure 20 shows the RSS under different distances. The RSS decreases as the user-device distance increases, indicating a weaker signal strength. This reduction in signal strength can lead to degraded SNR, and increased BP estimated errors.

**4.5.3 The Impact of FPS..** We evaluate the performance of our system under varying FPS settings, specifically 200, 100, 50, and 25, achieved through downsampling. Figure 21 illustrates the MAEs of SBP and DBP predictions at these FPS settings, resulting in 6.5 mmHg, 6.6 mmHg, 7.0 mmHg, and 11.6 mmHg for SBP, and 4.7 mmHg, 4.7 mmHg, 5.2 mmHg, and 5.3 mmHg for DBP, respectively. The result reveals that the improvement in BP prediction accuracy is slight when the FPS is set to 100 or higher. However, a dramatic decrease in prediction accuracy is

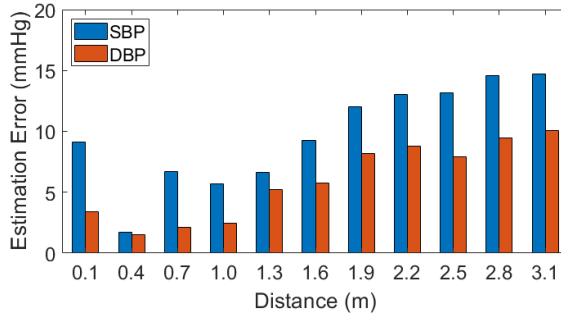


Fig. 19. Impact of different user-device distances.

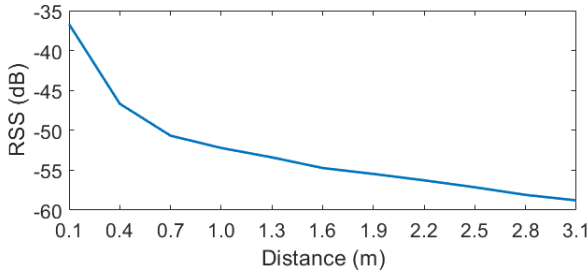


Fig. 20. RSS under different user-device distances.

observed at an FPS of 25. Consequently, in the context of BP monitoring, it is suggested to set the FPS to be greater than or equal to 100 to ensure the accuracy of BP prediction while balancing power consumption and data transmission requirements.

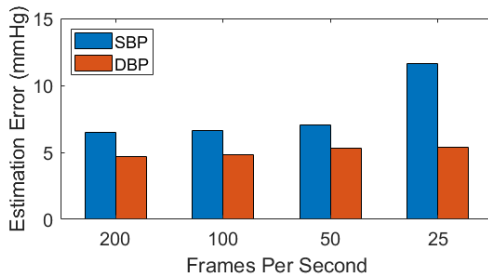


Fig. 21. Impact of different FPS.

**4.5.4 The Impact of Environmental Setup.** We conduct the experiments in four different rooms with different sizes and layouts. Figure 22 shows the estimated errors in the four rooms. The MAEs of SBP predicted by RF-BP are all less than 5 mmHg and the MAEs of DBP predicted by RF-BP are all less than 3 mmHg. There is no obvious difference in the four rooms. The reason is supposed to the fact that the clutter caused by static reflection in the environment are removed and RF-BP can identify the location of user accurately. It indicates that our system is not sensitive to the experimental environment.

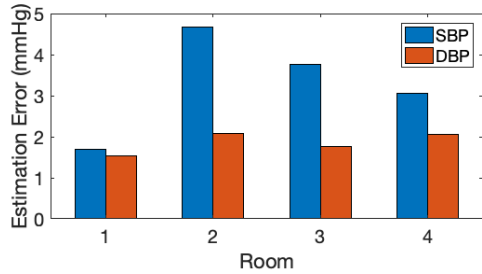


Fig. 22. Impact of environmental setup.

#### 4.6 Case Study

This study aims to demonstrate that our system is capable of accurately monitoring the BP of both normotensive users and hypertensive users and predicting the trend of BP effectively.

To provide an intuitive demonstration of the ability of RF-BP, we choose four users from our dataset to conduct the case study. Each user represents a different BP condition, allowing us to assess the accuracy in predicting BP and monitoring its trend. For each chosen user, we plot the waveform of the predicted and ground-truth BP in Figure 23. For user 1, the BP is within the normal range, that is, the SBP is around 100 mmHg and the DBP is around 60 mmHg, as shown in Figure 23a. The SBP of user 2 fluctuates around 140 mmHg, as shown in Figure 23b. Similarly, the SBP of user 3 gradually decreases from 160 mmHg to 140 mmHg, as shown in Figure 23c. Both of user 2 and user 3 suffer from systolic hypertension. The DBP of user 4 who suffers from diastolic hypertension, fluctuates around 110 mmHg, as shown in Figure 23d.

It can be seen that the BP predicted by RF-BP is consistent with the ground truth, which indicates that RF-BP can accurately predict a user's BP, no matter whether it is a user with normal blood pressure or systolic hypertension or diastolic hypertension. Moreover, the BP waveforms predicted by RF-BP align closely with the ground truth, confirming its capability to accurately monitor the trend of BP. This holds true for users with normal BP, systolic hypertension, or diastolic hypertension.

## 5 LIMITATIONS AND DISCUSSION

In this work, we focus on utilizing a UWB device to achieve regular daily monitoring of BP. We briefly discuss the limitations and also some promising future research directions below.

**Body motion.** In RF-BP, we discard the signals when the user is in a body-movement state. This approach is justified by the fact that our system can predict BP once it has captured 20 seconds of the stationary state in a seated user. Nevertheless, if BP can be effectively monitored even during body movement, it would significantly enhance the reliability of BP monitoring. In our future work, we plan to model the effect of body movements on the pulse waves, and design the corresponding algorithm to recover the pulse waves.

**Data distribution.** The self-built dataset comprises 60-hour data from a total of 70 users. The distribution of SBP and DBP exhibits a general resemblance to a normal distribution, thereby resulting in data imbalance. Specifically, BP can be predicted accurately for users with normal BP, whereas the accuracy of BP prediction is diminished for hypertensive users. It is worth noting that some difficulty exists in the collection of data from hypertensive patients. It is primarily due to the fact that a significant proportion of hypertensive patients have normal BP by taking antihypertensive medications. As the future work, we need to collect more hypertensive data from hypertensive patients to improve the accuracy of BP prediction.

**Co-existence issues with other RF technologies.** Multiple radio frequency technologies operating in the same environment may lead to interference or reduced performance. Therefore, it is essential to consider the possibility of co-existence issues with other RF technologies in the context of the proposed system. To ensure

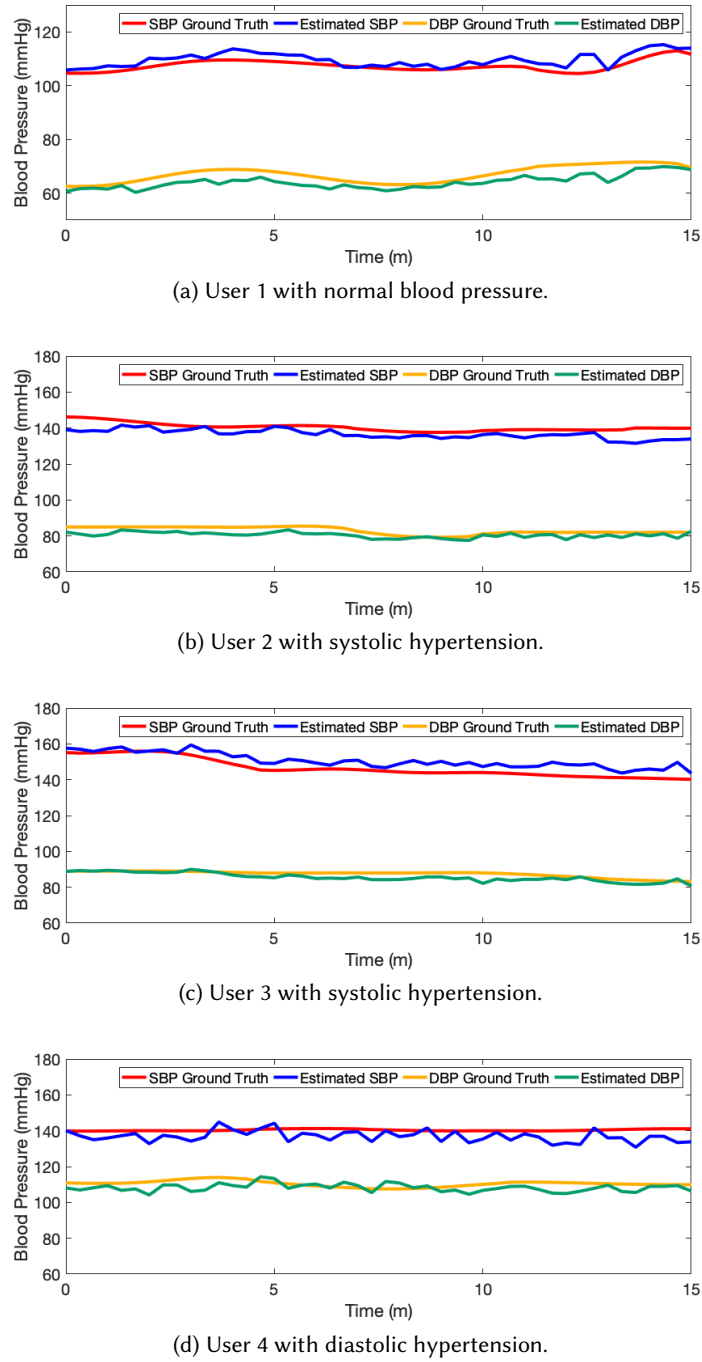


Fig. 23. Case study of blood pressure prediction.

that UWB devices operate with minimal interference with other radio services and technologies, the Federal Communications Commission (FCC) has established specific UWB standards, encompassing regulations related to power levels, emission limits, frequency bands, and interference mitigation. Specifically, the frequency band designated for UWB by FCC spans from  $3.1\text{ GHz}$  to  $10.6\text{ GHz}$ . Additionally, other countries have also established standards for using UWB signals. Taking our UWB device as an example, it operates within the frequency range of  $6.6\text{ GHz}$  to  $8\text{ GHz}$ . For common RF signals, Wi-Fi primarily operates in the  $2.4\text{ GHz}$  and  $5\text{ GHz}$  bands, Bluetooth typically utilizes the  $2.4\text{ GHz}$  band, and the frequency of mobile communication systems generally falls below  $2.6\text{ GHz}$ . This discrepancy in frequency ranges shows that our system is unlikely to be affected by co-existence issues with other RF technologies.

## 6 CONCLUSION

In this paper, we employ a UWB device to achieve regular daily monitoring of BP. At first, we design a human presence and state identification algorithm. Next, to capture quasi-pulse waves, we propose two methods that utilize peak detection and PCA to identify aliased and deformed parts in UWB signals, respectively. Further, we construct a deep learning model that incorporates a multi-scale feature extractor, a channel attention mechanism and residual connections to predict BP. Finally, we build the BP monitoring system named RF-BP and conduct extensive experiments to evaluate the performance of RF-BP. The experimental results show that RF-BP can accurately predict BP and monitor its trend. We believe that RF-BP can bring significant convenience to individuals' life and promote the monitoring of human health.

## ACKNOWLEDGMENTS

This work is supported by the National Natural Science Foundation of China under Grant No.62072450.

## REFERENCES

- [1] 2002. AAMI-SP10 Electronic or Automated Sphygmomanometers. <https://standards.globalspec.com/std/25451/SP10>.
- [2] 2023. Apple UWB U1 chip. <https://www.techinsights.com/blog/apple-u1-tmka75-ultra-wideband-uwb-chip-analysis>.
- [3] 2023. FITVII GT5 IP68 Waterproof SmartWatch with Heart Rate Blood Pressure Monitor. <https://fitvii.com/products/novae-black-ip68-waterproof-smart-watch>.
- [4] 2023. Google Pixel UWB. <https://www.qorvo.com/newsroom/news/2021/qorvo-delivers-ultra-wideband-in-google-pixel-6-pro>.
- [5] 2023. Heartguide wearable blood pressure monitor. <https://omronhealthcare.com/products/heartguide-wearable-blood-pressure-monitor-bp8000m/>.
- [6] 2023. HK-2000C. <http://www.hfhuake.com/chapinzhansi/yiliaochuanganqi/yadianshimaibochua/2014/1230/17.html>.
- [7] 2023. Holter monitoring of blood pressure. <https://www.medicum.ee/en/uuring/funktsoonaaldiagnostilised-uuringud/vererohu-holter-monitoring/>.
- [8] 2023. List of UWB-enabled mobile devices. [https://en.wikipedia.org/wiki/List\\_of\\_UWB-enabled\\_mobile\\_devices](https://en.wikipedia.org/wiki/List_of_UWB-enabled_mobile_devices).
- [9] 2023. Omron HEM-7132 Blood Pressure Monitor with Fit Cuff. <https://www.amazon.in/Omrone-HEM-7132-Blood-Pressure-Monitor/dp/B00FVW7T6U>.
- [10] 2023. Samsung UWB chipset. <https://news.samsung.com/global/samsung-announces-ultra-wideband-chipset-with-centimeter-level-accuracy-for-mobile-and-automotive-devices>.
- [11] 2023. WHO Hypertension. <https://www.who.int/data/gho/indicator-metadata-registry/imr-details/3155>.
- [12] 2023. Xiaomi UWB technology. <https://www.nxp.com/company/about-nxp/nxp-trimension-ultra-wideband-technology-powers-xiaomi-mix4-smartphone-to-deliver-new-point-to-connect-smart-home-solution:NW-NXP-TRIMENSION-ULTRA-WIDEBAND-TECHNOLOGY-POWERS>.
- [13] John Allen. 2007. Photoplethysmography and its application in clinical physiological measurement. *Physiological measurement* 28, 3 (2007), R1.
- [14] J Crighton Bramwell and Archibald Vivian Hill. 1922. The velocity of pulse wave in man. *Proceedings of the Royal Society of London. Series B, Containing Papers of a Biological Character* 93, 652 (1922), 298–306.
- [15] Chun-Fu Richard Chen, Quanfu Fan, and Rameswar Panda. 2021. Crossvit: Cross-attention multi-scale vision transformer for image classification. In *Proceedings of the IEEE/CVF international conference on computer vision*. 357–366.

- [16] Younhee Choi, Qiao Zhang, and Seokbum Ko. 2013. Noninvasive cuffless blood pressure estimation using pulse transit time and Hilbert–Huang transform. *Computers & Electrical Engineering* 39, 1 (2013), 103–111.
- [17] Chadi El-Hajj and Panayiotis A Kyriacou. 2021. Deep learning models for cuffless blood pressure monitoring from PPG signals using attention mechanism. *Biomedical Signal Processing and Control* 65 (2021), 102301.
- [18] Andrea Galassi, Marco Lippi, and Paolo Torroni. 2020. Attention in natural language processing. *IEEE transactions on neural networks and learning systems* 32, 10 (2020), 4291–4308.
- [19] Surendhra Goli and T Jayanthi. 2014. Cuff less continuous non-invasive blood pressure measurement using pulse transit time measurement. *Int. J. Recent Dev. Eng. Technol* 2, 1 (2014), 16–86.
- [20] Unsoo Ha, Salah Assana, and Fadel Adib. 2020. Contactless seismocardiography via deep learning radars. In *Proceedings of the 26th annual international conference on mobile computing and networking*. 1–14.
- [21] Minju Han, Young-Ro Lee, Taeyoung Park, Sang-Hyun Ihm, Wook Bum Pyun, Thilo Burkard, Myeong-Chan Cho, Miguel Camafort, Eugene Yang, George S Stergiou, et al. 2023. Feasibility and measurement stability of smartwatch-based cuffless blood pressure monitoring: A real-world prospective observational study. *Hypertension Research* 46, 4 (2023), 922–931.
- [22] Mi He, Yongjian Nian, Luping Xu, Lihong Qiao, and Wenwu Wang. 2020. Adaptive separation of respiratory and heartbeat signals among multiple people based on empirical wavelet transform using UWB radar. *Sensors* 20, 17 (2020), 4913.
- [23] Dichao Hu. 2020. An introductory survey on attention mechanisms in NLP problems. In *Intelligent Systems and Applications: Proceedings of the 2019 Intelligent Systems Conference (IntelliSys) Volume 2*. Springer, 432–448.
- [24] Lun Huang, Wenmin Wang, Jie Chen, and Xiao-Yong Wei. 2019. Attention on attention for image captioning. In *Proceedings of the IEEE/CVF international conference on computer vision*. 4634–4643.
- [25] DJ Hughes, Charles F Babbs, LA Geddes, and JD Bourland. 1979. Measurements of Young’s modulus of elasticity of the canine aorta with ultrasound. *Ultrasonic imaging* 1, 4 (1979), 356–367.
- [26] Josep Maria Solà i Carós and Josep Maria. 2011. *Continuous non-invasive blood pressure estimation*. Ph.D. Dissertation. ETH.
- [27] Marie Jung, Michael Caris, and Stephan Stanko. 2021. Non-contact blood pressure estimation using a 300 GHz continuous wave radar and machine learning models. In *2021 IEEE International Symposium on Medical Measurements and Applications (MeMeA)*. IEEE, 1–6.
- [28] Usman Mahmood Khan, Zain Kabir, Syed Ali Hassan, and Syed Hassan Ahmed. 2017. A deep learning framework using passive WiFi sensing for respiration monitoring. In *GLOBECOM 2017-2017 IEEE Global Communications Conference*. IEEE, 1–6.
- [29] Fatema-Tuz-Zohra Khanam, Ali Al-Naji, and Javaan Chahl. 2019. Remote monitoring of vital signs in diverse non-clinical and clinical scenarios using computer vision systems: A review. *Applied Sciences* 9, 20 (2019), 4474.
- [30] Ch Kitiyakara and NJ Guzman. 1998. Malignant hypertension and hypertensive emergencies. *Journal of the American society of nephrology* 9, 1 (1998), 133–142.
- [31] von DJ Korteweg. 1878. Ueber die Fortpflanzungsgeschwindigkeit des Schalles in elastischen Röhren. *Annalen der Physik* 241, 12 (1878), 525–542.
- [32] Yonggu Lee, Jun-Young Park, Yeon-Woo Choi, Hyun-Kyung Park, Seok-Hyun Cho, Sung Ho Cho, and Young-Hyo Lim. 2018. A novel non-contact heart rate monitor using impulse-radio ultra-wideband (IR-UWB) radar technology. *Scientific reports* 8, 1 (2018), 13053.
- [33] Mingai Li, Ruotu Wang, Jinfu Yang, Lijuan Duan, et al. 2019. An improved refined composite multivariate multiscale fuzzy entropy method for MI-EEG feature extraction. *Computational intelligence and neuroscience* 2019 (2019).
- [34] Siheng Li, Zhi Wang, Beihong Jin, Fusang Zhang, Xiaoyong Ren, and Yitong Zhang. 2022. Sleep Respiration Monitoring Using Attention-reinforced Radar Signals. In *2022 IEEE International Conference on Bioinformatics and Biomedicine (BIBM)*. IEEE, 1612–1615.
- [35] Siheng Li, Zhi Wang, Fusang Zhang, and Beihong Jin. 2021. Fine-grained respiration monitoring during overnight sleep using IR-UWB radar. In *International Conference on Mobile and Ubiquitous Systems: Computing, Networking, and Services*. Springer, 84–101.
- [36] Xin Li, Jun Xu, Jin Hua Duan, and Leng Han. 2012. Design of Electronic Sphygmomanometer Based on Oscillography. *Applied Mechanics and Materials* 236 (2012), 850–855.
- [37] Xiang Li, Wei Zhang, and Qian Ding. 2019. Deep learning-based remaining useful life estimation of bearings using multi-scale feature extraction. *Reliability engineering & system safety* 182 (2019), 208–218.
- [38] Xin Liu, Josh Fromm, Shwetak Patel, and Daniel McDuff. 2020. Multi-task temporal shift attention networks for on-device contactless vitals measurement. *Advances in Neural Information Processing Systems* 33 (2020), 19400–19411.
- [39] Simon Lyra, Leon Mayer, Liyang Ou, David Chen, Paddy Timms, Andrew Tay, Peter Y Chan, Bergita Ganse, Steffen Leonhardt, and Christoph Hoog Antink. 2021. A deep learning-based camera approach for vital sign monitoring using thermography images for ICU patients. *Sensors* 21, 4 (2021), 1495.
- [40] Taiga Nabeshima, Thanh-Vinh Nguyen, and Hidetoshi Takahashi. 2022. Frequency Characteristics of Pulse Wave Sensor Using MEMS Piezoresistive Cantilever Element. *Micromachines* 13, 5 (2022), 645.
- [41] Ross Nye, Zhe Zhang, and Qiang Fang. 2015. Continuous non-invasive blood pressure monitoring using photoplethysmography: A review. In *2015 International Symposium on Bioelectronics and Bioinformatics (ISBB)*. IEEE, 176–179.
- [42] Eoin O’Brien, James Petrie, William Littler, Michael De Swiet, Paul L Padfield, Douglas Altman, Martin Bland, Andrew Coats, Neil Atkins, et al. 1993. The British Hypertension Society protocol for the evaluation of blood pressure measuring devices. *J hypertens* 11,

- Suppl 2 (1993), S43–S62.
- [43] CCY Poon and YT Zhang. 2006. Cuff-less and noninvasive measurements of arterial blood pressure by pulse transit time. In *2005 IEEE engineering in medicine and biology 27th annual conference*. IEEE, 5877–5880.
  - [44] Solmaz Rastegar, Hamid Gholam Hosseini, and Andrew Lowe. 2023. Hybrid CNN-SVR Blood Pressure Estimation Model Using ECG and PPG Signals. *Sensors* 23, 3 (2023), 1259.
  - [45] Vignesh Ravichandran, Balamurali Murugesan, Vaishali Balakarthikeyan, Keerthi Ram, SP Preejith, Jayaraj Joseph, and Mohanasankar Sivaprakasam. 2019. RespNet: A deep learning model for extraction of respiration from photoplethysmogram. In *2019 41st annual international conference of the IEEE engineering in medicine and biology society (EMBC)*. IEEE, 5556–5559.
  - [46] Ali Raza, Arif Mehmood, Saleem Ullah, Maqsood Ahmad, Gyu Sang Choi, and Byung-Won On. 2019. Heartbeat sound signal classification using deep learning. *Sensors* 19, 21 (2019), 4819.
  - [47] Lingyun Ren, Haofei Wang, Krishna Naishadham, Ozlem Kilic, and Aly E Fathy. 2016. Phase-based methods for heart rate detection using UWB impulse Doppler radar. *IEEE Transactions on Microwave Theory and Techniques* 64, 10 (2016), 3319–3331.
  - [48] Ariel Roguin. 2006. Scipione Riva-Rocci and the men behind the mercury sphygmomanometer. *International journal of clinical practice* 60, 1 (2006), 73–79.
  - [49] Sven Schellenberger, Kilin Shi, Tobias Steigleider, Anke Malessa, Fabian Michler, Laura Hameyer, Nina Neumann, Fabian Lurz, Robert Weigel, Christoph Ostgatthe, et al. 2020. A dataset of clinically recorded radar vital signs with synchronised reference sensor signals. *Scientific data* 7, 1 (2020), 291.
  - [50] Iman Sharifi, Sobhan Goudarzi, and Mohammad Bagher Khodabakhshi. 2019. A novel dynamical approach in continuous cuffless blood pressure estimation based on ECG and PPG signals. *Artificial intelligence in medicine* 97 (2019), 143–151.
  - [51] Haotian Shi, Jiasheng Pan, Zhi Zheng, Bo Wang, Cheng Shen, and Yongxin Guo. 2022. Radar-based blood pressure estimation using multiple features. In *2022 IEEE MTT-S International Microwave Biomedical Conference (IMBioC)*. IEEE, 183–185.
  - [52] Zhenguo Shi, Tao Gu, Yu Zhang, and Xi Zhang. 2022. mmBP: Contact-Free Millimetre-Wave Radar Based Approach to Blood Pressure Measurement. In *Proceedings of the 20th ACM Conference on Embedded Networked Sensor Systems*. 667–681.
  - [53] Monika Simjanoska, Martin Gjoreski, Matjaž Gams, and Ana Madevska Bogdanova. 2018. Non-invasive blood pressure estimation from ECG using machine learning techniques. *Sensors* 18, 4 (2018), 1160.
  - [54] Mohd Zubir Suboh, Rosmina Jaafar, Nazrul Anuar Nayan, Noor Hasmiza Harun, and Mohd Shawal Faizal Mohamad. 2022. Analysis on four derivative waveforms of photoplethysmogram (PPG) for fiducial point detection. *Frontiers in Public Health* 10 (2022), 920946.
  - [55] Ying Sun, Yaoqing Weng, Bowen Luo, Gongfa Li, Bo Tao, Du Jiang, and Disi Chen. 2023. Gesture recognition algorithm based on multi-scale feature fusion in RGB-D images. *IET Image Processing* 17, 4 (2023), 1280–1290.
  - [56] Swaroop Venkatesh, Christopher R Anderson, Natalia V Rivera, and R Michael Buehrer. 2005. Implementation and analysis of respiration-rate estimation using impulse-based UWB. In *MILCOM 2005-2005 IEEE Military Communications Conference*. IEEE, 3314–3320.
  - [57] Nastassia Vysotskaya, Christoph Will, Lorenzo Servadei, Noah Maul, Christian Mandl, Merlin Nau, Jens Harnisch, and Andreas Maier. 2023. Continuous Non-Invasive Blood Pressure Measurement Using 60 GHz-Radar—A Feasibility Study. *Sensors* 23, 8 (2023), 4111.
  - [58] Qing Wang, Weimin Lyu, Zhi Cheng, and Changyuan Yu. 2023. Noninvasive Measurement of Vital Signs with the Optical Fiber Sensor Based on Deep Learning. *Journal of Lightwave Technology* (2023).
  - [59] Zhi Wang, Beihong Jin, Siheng Li, Fusang Zhang, and Wenbo Zhang. 2023. ECG-grained Cardiac Monitoring Using UWB Signals. *Proceedings of the ACM on Interactive, Mobile, Wearable and Ubiquitous Technologies* 6, 4 (2023), 1–25.
  - [60] Li Wen, Shuqin Dong, Zhi Zhang, Changzhan Gu, and Junfa Mao. 2022. Noninvasive continuous blood pressure monitoring based on wearable radar sensor with preliminary clinical validation. In *2022 IEEE/MTT-S International Microwave Symposium-IMS 2022*. IEEE, 707–710.
  - [61] Zongxing Xie, Hanrui Wang, Song Han, Elinor Schoenfeld, and Fan Ye. 2022. DeepVS: a deep learning approach for RF-based vital signs sensing. In *Proceedings of the 13th ACM international conference on bioinformatics, computational biology and health informatics*. 1–5.
  - [62] Sungwon Yoo, Shahzad Ahmed, Sun Kang, Duhyun Hwang, Jungjun Lee, Jungduck Son, and Sung Ho Cho. 2021. Radar recorded child vital sign public dataset and deep learning-based age group classification framework for vehicular application. *Sensors* 21, 7 (2021), 2412.
  - [63] Shujie Zhang, Tianyue Zheng, Zhe Chen, and Jun Luo. 2022. Can We Obtain Fine-grained Heartbeat Waveform via Contact-free RF-sensing?. In *IEEE INFOCOM 2022-IEEE conference on computer communications*. IEEE, 1759–1768.
  - [64] Hengshuang Zhao, Jiaya Jia, and Vladlen Koltun. 2020. Exploring self-attention for image recognition. In *Proceedings of the IEEE/CVF conference on computer vision and pattern recognition*. 10076–10085.
  - [65] Bin Zhou, Rodrigo M Carrillo-Larco, Goodarz Danaei, Leanne M Riley, Christopher J Paciorek, Gretchen A Stevens, Edward W Gregg, James E Bennett, Bethlehem Solomon, Rosie K Singleton, et al. 2021. Worldwide trends in hypertension prevalence and progress in treatment and control from 1990 to 2019: a pooled analysis of 1201 population-representative studies with 104 million participants. *The Lancet* 398, 10304 (2021), 957–980.
  - [66] Domenico Zito, Domenico Pepe, Martina Mincica, Fabio Zito, Alessandro Tognetti, Antonio Lanatà, and Danilo De Rossi. 2011. SoC CMOS UWB pulse radar sensor for contactless respiratory rate monitoring. *IEEE transactions on biomedical circuits and systems* 5, 6 (2011), 503–510.